Environment-Induced Exciton Renormalization in the Photosystem II Reaction Center

Tucker Allen,*,† Barry Y. Li,† Nadine C. Bradbury,‡ and Daniel Neuhauser†

†*Department of Chemistry and Biochemistry, University of California, Los Angeles, Los Angeles, CA, 90095, USA*

‡*Department of Chemistry, Princeton University, Princeton, NJ, 08544, USA*

E-mail: tuckerallen27@ucla.edu

Date: February 23, 2026

Abstract

Protein electrostatics tune excitation energies in the Photosystem II reaction center (PSII-RC), yet a fully quantum-mechanical many-body description of how the surrounding protein environment renormalizes excitons has remained computationally inaccessible. The Bethe-Salpeter equation (BSE) within many-body perturbation theory accurately describes excitonic physics through an explicit electron-hole interaction, but is prohibitively expensive for systems containing thousands of valence electrons. Here, we show that for sufficiently large systems the BSE becomes simpler to solve when treated with modern stochastic sampling techniques, as atomistic interactions self-average. In this regime, the effective electron-hole interaction mediated by the environment is governed by collective k-dependent polarization. These insights enable an *ab initio* study of the PSII-RC in which all six chlorins forming the hexameric dye core are treated explicitly together with a roughly seven Angstrom local protein environment. We directly compare the low-lying optical excitations of the isolated

chromophore hexamer (1276 valence electrons) and the protein-dye cluster (3238 valence electrons). For Q_y excitations near 680 nm, inclusion of the protein environment induces polarization-dependent energy shifts, redistributes spectral weight, and alters exciton delocalization and pigment character. Lateral and transverse asymmetries in the low-lying excited states are captured at the BSE level of theory. These results establish that we now have the tools for many-body calculations of biological nanostructures.

Photosystem II (PSII) is a nanoscale molecular machine embedded in the thylakoid membranes of plants, algae, and cyanobacteria. Oxygenic photosynthesis begins at the reaction center of PSII (PSII-RC), where incident photons from sunlight are absorbed by a network of chromophores, generating electron-hole pairs (excitons) and initiating a charge-transfer cascade. Energy transfer drives water splitting and supplies electrons to the photosynthetic electron transport chain. Water oxidation produces molecular oxygen essential for life, as well as reducing equivalents that enable the conversion of carbon dioxide into simple sugars.[1,2] The atomic structure and pigment arrangement of the PSII-RC are now well resolved at near-atomic resolution.[3] Despite this well-established biochemical pathway and detailed structural knowledge, understanding of the electronic structure of the initial photoexcited states and their sensitivity to the surrounding protein environment remains limited. Further, primary charge separation occurs with near-unity quantum efficiency, making an atomistic, many-body understanding of the PSII-RC essential for uncovering design principles for photovoltaic devices and artificial photosynthesis.[4,5]

Theoretical descriptions of the PSII-RC have historically relied on effective excitonic Hamiltonians that capture energy transfer between pigments in a simplified manner while treating the surrounding protein implicitly.[6,7] These approaches have provided a useful conceptual picture of exciton energy transfer but neglect the explicit electronic response of the protein environment. More detailed insight has come from mixed quantum-classical approaches, including QM/MM frameworks that employ high-level quantum chemistry meth-

ods, such as coupled-cluster theory, alongside range-separated hybrid (RSH) time-dependent density-functional theory (TDDFT).[8–11] These studies have elucidated the role of protein electrostatics, structural disorder, and protein dynamics in shaping excitation energies and charge-transfer pathways. For example, QM/MM studies have shown that the protein electrostatic environment induces transverse and lateral asymmetries that favor charge separation along the D1 branch of the pigment-protein complex.[8,12] However, environmental screening is typically described at a classical or semi-classical level and the chromophoric complex is rarely treated as a collective supramolecular electronic system.

For a fully quantum-mechanical treatment, TDDFT has become a widely used tool for excited-state calculations in large photosynthetic complexes. Explicit TDDFT calculations treating the PSII-RC chromophores as a single supramolecular complex were first demonstrated by Frankcombe using the CAM-B3LYP exchange-correlation (XC) functional.[13] Subsequent work by Kavanagh *et al.* reported the largest PSII-RC TDDFT model to date, incorporating both the full chromophoric complex and nearby protein residues.[14] With highly optimized implementations, TDDFT enables simulations of systems containing thousands of atoms. At the same time, the accuracy of TDDFT and its treatment of many-body effects are fundamentally limited by the choice of XC functional. In heterogeneous systems such as PSII, long-range electron-hole interactions and anisotropic dielectric screening are difficult to capture within local or semilocal approximations to the XC functional, and charge-transfer excitations remain a persistent challenge.[15] RSH XC functionals improve the description of long-range effects but incur substantial additional cost associated with the evaluation of hybrid exchange.[16–19] Further, the use of a single range-separation parameter across chemically distinct regions of the complex constrains the ability to properly describe screening. In addition, common tuning procedures are not size-extensive, although a recent density-based tuning strategy has been proposed.[20]

Many-body perturbation theory (MBPT), and in particular the Bethe-Salpeter equation (BSE), provides a more explicit treatment of excitonic effects through a screened electron-

hole interaction. In simple terms, the BSE, under the static approximation, is equivalent to time-dependent Hartree Fock (TDHF) with a modified exchange term, where the effective interaction:[21–23]

$$W(r, r', \omega = 0) = \epsilon^{-1}(r, r')v(r - r'), \tag{1}$$

replaces the bare Coulomb interaction. However, constructing W via Eq.(1) is computationally prohibitive for systems with several thousand valence electrons. Even within the static approximation, building the screened Coulomb matrix requires explicit summations over many occupied and unoccupied states to form the irreducible polarizability, followed by dense matrix operations to obtain the inverse dielectric function. The resulting scaling and memory costs typically restrict BSE calculations to systems far smaller than realistic photosynthetic complexes, although applications to individual chlorophylls and small pigment assemblies have been reported.[24,25]

Recent efforts have begun to push the system-size limits of approaches that incorporate screened electron-hole interactions. Work by Förster and Visscher employed a quasiparticle self-consistent GW (qpGW)-BSE approach to model the full PSII-RC with nearly 2000 electrons, using a pair-atomic density-fitting procedure for matrix elements of Eq.(1).[26] Further, our recently developed mixed deterministic and sparse-stochastic long-range hybrid TDDFT approach[27] enables simulations of similar size and beyond. However, there remains a need to go beyond treating the chromophoric complex alone by incorporating explicit protein environments and simultaneously including electron-hole screening beyond the traditional tuned RSH-TDDFT level.

Here, we adopt an alternative approach that avoids building and storing the screened Coulomb elements explicitly. Specifically, we employ our recently developed screened time-dependent Hartree Fock-like method, TDHF@v_W,[28] which replaces the exact screened Coulomb operator, $W(r, r')$, with a translationally invariant screened exchange kernel, $v_W(r-r')$. This assumption reflects the fact that for large systems, it is the overall k-dependent polarization, not individual atom-atom interactions, that is important. The effective kernel v_W is

constructed via a least-squares fitting procedure, obtained from independent applications of Eq.(1) to randomly sampled orbital-pair densities; the expansion converges rapidly with the number of pair densities. Acting by W is efficiently calculated through real-time grid-based stochastic time-dependent Hartree dynamics.[28–31] This technique replaces the time-evolution of all occupied orbitals with a small set of stochastic states that are each a random linear-combination of all occupied orbitals. This then provides the k-space resolved polarization field that has a non-trivial dependence on k, and cannot be captured with conventional RSH functionals.

The translationally invariant $v_W(r-r')$ concept is similar to the bootstrap XC-kernel approach developed by Gross and co-workers for periodic solids.[32] The TDHF@v_W framework has previously yielded accurate optical gaps across a broad class of conjugated molecular systems, including polymethine cyanine dyes as well as planar and curved aromatic hydrocarbons.[28,33]

Combined with mixed deterministic and sparse-stochastic compression of exchange integrals,[34,35] TDHF@v_W avoids explicit orbital summations and reduces the cost of screened exchange, enabling fully quantum-mechanical simulations of biomolecular systems with thousands of valence electrons. Further, through an efficient iterative approach to diagonalizing the two-particle Hamiltonian, we go beyond the Tamm-Dancoff approximation and assess the role of resonant-antiresonant coupling in environment-induced exciton renormalization.[36]

In this article, we make a direct, fully quantum-mechanical comparison between the isolated PSII-RC chromophore hexamer (1276 valence electrons, analogous to the work in Refs.[26,27]) and the same pigment core embedded in a roughly seven Angstrom environment comprising axial histidine ligands, nearby residues, and protein-bound plastoquinones (3238 valence electrons). This enables us to illustrate clearly how the environment reshapes the low-lying excitons in the PSII-RC. The protein-embedded PSII-RC consists of 1331 atoms and is, to our knowledge, the largest to date model of PSII that is treated with beyond-TDDFT methods. Methodological details are provided in the Supplemental Information (SI).

We present in the results section the polarization-resolved optical spectra, exciton energies, transition densities, and participation ratios. These observables quantify how anisotropic environmental screening redistributes spectral weight, shifts excitation energies, and modifies exciton delocalization and pigment character. Finally, in the conclusions section we discuss the implications of the new capabilities to simulate large quantum biological systems, and then discuss future directions.

Results and Discussion

Fig. 1 shows the optimized protein-embedded PSII-RC with explicitly treated pigments, residues, and cofactors, with their names and positions indicated. In Table 1, the RSH-DFT bandgaps are provided, and we observe a 0.1 eV gap reduction upon protein embedding.

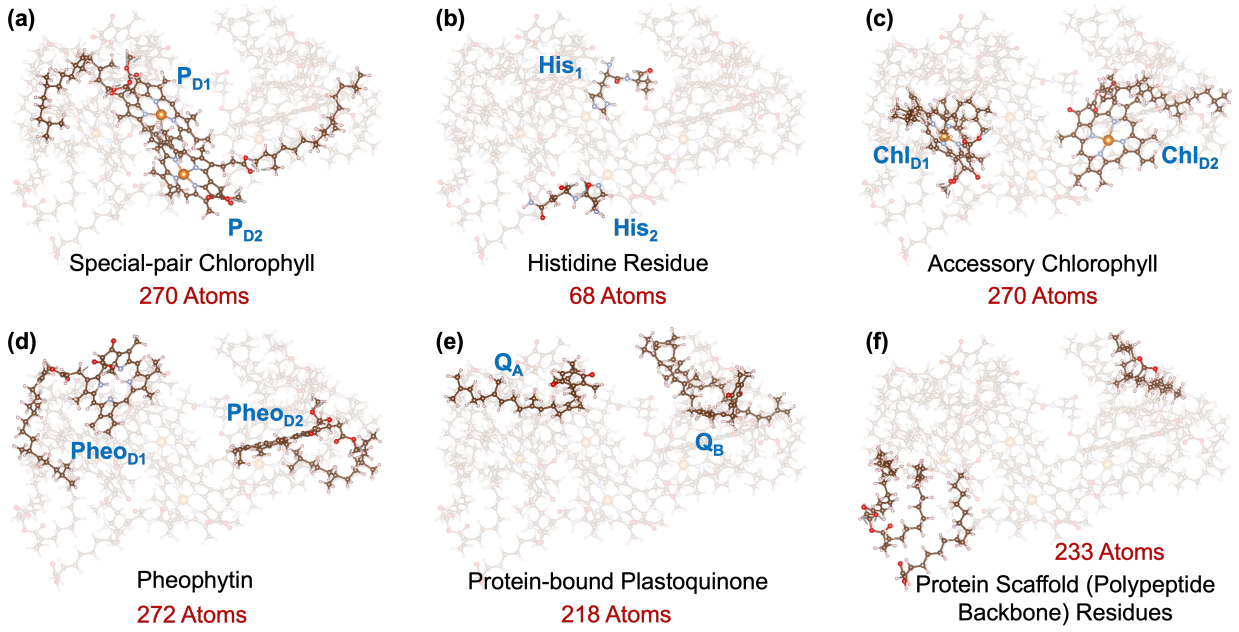

Figure 1: Optimized protein-embedded PSII-RC (overall 1331 atoms) with specific segments highlighted: **(a)** special-pair chlorophylls with Mg centers (P_{D1} and P_{D2}), 270 atoms; **(b)** histidine residues (with backbone) providing axial coordination to the Mg centers of P_{D1} and P_{D2}, 68 atoms; **(c)** accessory chlorophylls with Mg centers (Chl_{D1} and Chl_{D2}), 270 atoms; **(d)** pheophytins with hydrogen-coordinated macrocycles ($Pheo_{D1}$ and $Pheo_{D2}$), 272 atoms; **(e)** protein-bound plastoquinone cofactors (Q_A and Q_B), 218 atoms; **(f)** surrounding protein scaffold residues (polypeptide backbone), 233 atoms.

Table 1: Grid information (an isotropic grid-spacing of $dx = dy = dz = 0.5$ Bohr is used), number of occupied orbitals, CAM-LDA0 DFT bandgaps, N_v valence and N_c conduction orbitals used in spectral calculations, and $N_{k_{\text{low}}}$: the number of deterministically treated long-wavelength terms for exchange integrals. The compressed high-k space is represented with 5000 sparse-stochastic vectors, which are sufficient for convergence.

System	N_x	N_y	N_z	dx	N_{occ}	DFT Gap	N_v	N_c	$N_{k_{\text{low}}}$
Isolated PSII-RC	136	132	124	0.5	638	3.51 eV	200	400	4683
Embedded PSII-RC	168	180	158	0.5	1619	3.41 eV	200	400	10091

Stochastic time-dependent Hartree propagation is separately performed for the isolated and protein-embedded PSII-RC. The size of the stochastic basis is $N_\beta = 1100$ and 800, respectively, for the isolated and protein-embedded PSII-RC. Due to self-averaging, the number of samples required to obtain a converged $v_W(k)$ potential tends to decrease with system size.

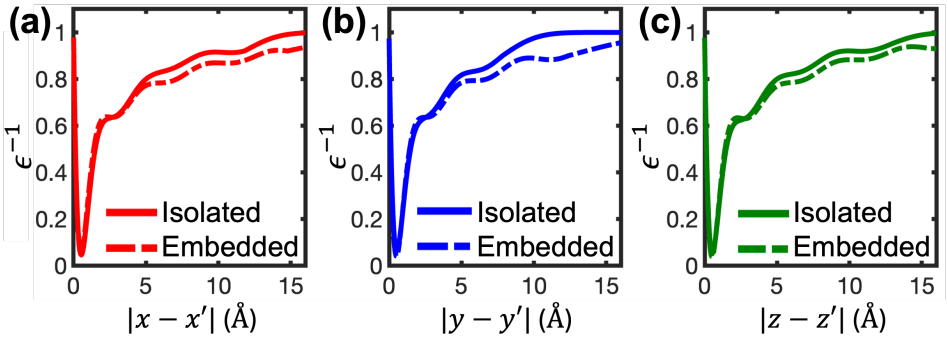

Figure 2: Real-space inverse dielectric functions for the isolated and protein-embedded PSII-RC, evaluated along Cartesian rays from the origin. Panels (a)–(c) show one-dimensional cuts where (a) $|x - x'|$ is varied with $y - y' = z - z' = 0$, (b) $|y - y'|$ is varied with $x - x' = z - z' = 0$, and (c) $|z - z'|$ is varied with $x - x' = y - y' = 0$.

From the attenuated exchange kernel, v_W, we form the inverse dielectric function, $\epsilon^{-1}(k) = 1 + v_W(k)/v(k)$, where $v(k)$ is the full (unscreened) non-periodic Coulomb interaction (see SI for details).[37] After the Fourier transform, the real-space inverse dielectric is obtained, as shown in Fig. 2. At short spatial-range, i.e., large reciprocal lattice vector k, the screening behavior is very similar between the isolated and embedded systems. At spatial separations of roughly 5 Å or more, we observe deviations in exchange attenuation between the two

systems. It is at large interelectronic distances (low-k) that screening is enhanced in the protein-embedded cluster.

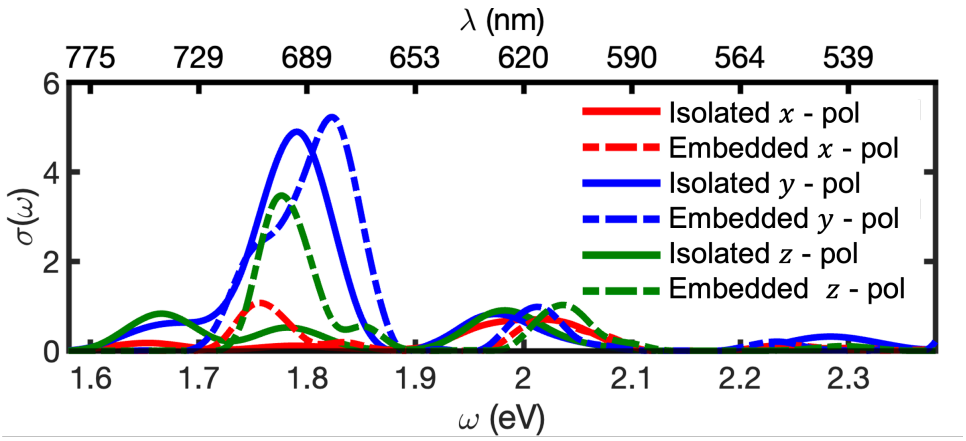

Figure 3: Polarization-resolved full TDHF@v_W optical spectra for the isolated and protein-embedded PSII-RC systems. Both systems use a transition space of $N_v = 200$ and $N_c = 400$ orbitals. Laser polarization directions are denoted as x-pol, y-pol, and z-pol.

Fig. 3 shows the polarization-resolved optical absorption spectra for the isolated and protein-embedded PSII-RC. To converge the spectral shapes below 3 eV in both systems, it is sufficient to use a transition-space of $N_v = 200$ valence and $N_c = 400$ conduction orbitals; we have confirmed that going beyond $N_c = 400$ does not shift peak positions by more than 0.01 eV. The absolute peak positions are then extrapolated to $N_v = N_{\text{occ}}$ and $N_c = 2N_{\text{occ}}$ by a simple linear fitting of the excitation energies as a function of $1/N_v$. Spectra provided in Fig. 3 are shifted to include this extrapolation. Details on the fitting are provided in the SI.

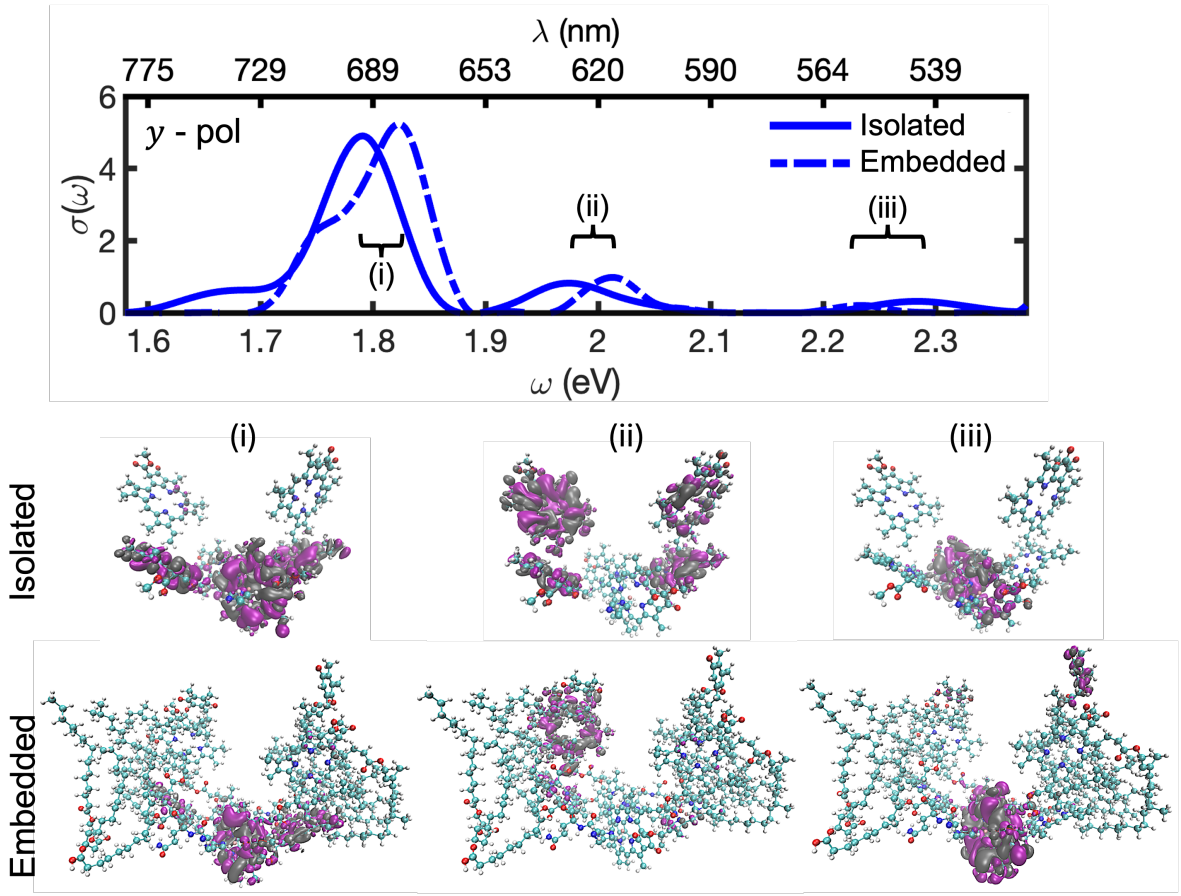

Figure 4: The y-polarized TDHF@v_W spectra for the isolated and protein-embedded PSII-RC, together with the transition density isosurfaces corresponding to the three dominant absorption peaks in both systems, labeled as **(i)**, **(ii)**, and **(iii)**. Isovalues of ± 0.00005 Bohr$^{-3/2}$ are used for all transition densities with purple used for positive values and grey for negative values.

The three lowest y-polarized excited states and associated transition densities are shown in Fig. 4. Table 2 summarizes the chromophoric character of each exciton and its participation ratio (PR), which describes the effective number of valence-to-conduction orbital transitions involved for an excitation at a sampled frequency ω. Peak (i) is the bright Q_y band excitation, with a peak position of 1.79 eV for the isolated PSII-RC that is blue-shifted by 0.03 eV upon protein-embedding. We observe a reduction in the PR upon embedding, indicating an environment-induced localization. The theoretical absorption peak of 1.82 eV (681 nm) for the embedded PSII-RC is in excellent agreement with the experimental absorption of 1.83 eV (679 nm) reported in.[14]

Table 2: Exciton characteristics of the four selected optical excitations (labeled in Figs. 4 and 5) of the isolated and protein-embedded PSII-RC. Listed are the excitation energies, dominant pigment contributions, and participation ratio (PR).

Exciton	System	Energy (eV)	Dominant Character	PR
(i)	Isolated	1.79	$P_{D2}/Chl_{D1}/Chl_{D2}$	15.3
	Embedded	1.82	$P_{D2}/Chl_{D1}/Chl_{D2}$	8.6
(ii)	Isolated	1.98	$Pheo_{D1}/Pheo_{D2}/Chl_{D1}/Chl_{D2}$	4.4
	Embedded	2.01	$Pheo_{D1}$	3.5
(iii)	Isolated	2.29	P_{D1}/P_{D2}	3.0
	Embedded	2.23	P_{D1}/P_{D2}, partial Q_A/Q_B	3.7
(iv)	Isolated	1.67	$Pheo_{D1}/Pheo_{D2}$	5.8
	Embedded	1.77	$Pheo_{D1}/Pheo_{D2}/P_{D1}$	7.9

Peaks (ii) and (iii) in Fig. 4 have lower absorption cross-sections than (i), but exhibit interesting changes in chromophore character upon the inclusion of local protein environment. Peak (ii) shows a delocalized excited state with transition-density amplitude across both pheophytins and accessory chlorophyll pigments. For the embedded PSII-RC, the peak is blue-shifted and the transition-density is more localized on the D1 branch of the complex. This is consistent with protein electrostatics inducing lateral asymmetry that favors the D1 branch of the pigment-protein complex.[8] Peak (iii) for the isolated PSII-RC has transition-density on the central P_{D1}/P_{D2} chlorophyll pair. With explicit environment, the peak is slightly red-shifted and a non-zero amplitude appears on the Q_A/Q_B plastoquinones.

In Fig. 5, the z-polarized absorption onset is provided. A weak doublet is observed in the spectrum for the isolated PSII-RC with transition-density localized on the pheophytins. For the embedded PSII-RC, we observe a 0.1 eV blue-shift and an enhancement in the absorption cross-section of the left peak. There is a borrowing of spectral weight from higher excitations, with the environment making the transition more dipole-allowed. The PR is slightly increased, and transition-density amplitude appears on the P_{D1} central chlorophyll.

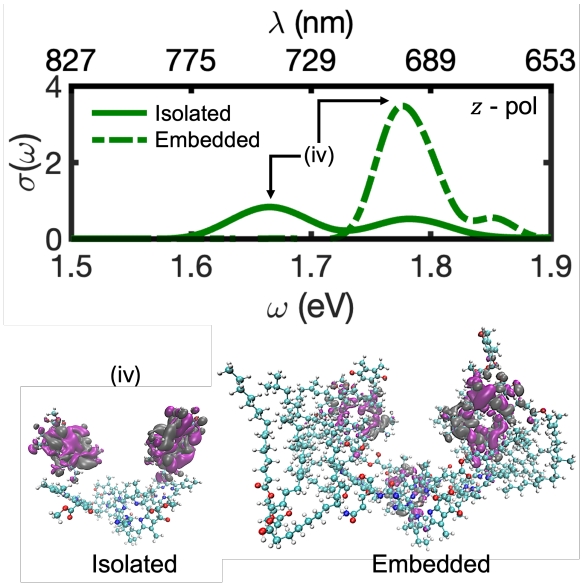

Figure 5: Same as Fig. 4, but for the z-polarization and the first absorption peak, labeled as **(iv)**.

To assess the role of resonant-antiresonant coupling on exciton renormalization in the PSII-RC, separate Tamm-Dancoff approximation (TDA) TDHF@v_W calculations were performed. In the TDA, peaks (i)-(iv) are rigidly blue-shifted compared with the full TDHF@v_W simulations. Additionally, we do not see noticeable changes in the transition-density characters. However, in the TDA, peak (i) does not blue-shift upon protein embedding. Additionally, peak (ii) does not red-shift. The environment-induced shifts are signatures of transverse anisotropy, and completely missed by the TDA. This signifies that transverse asymmetries in the PSII-RC are attributed to off-diagonal screened exchange interactions. Details of the TDA results are in the SI.

Conclusions

In summary, we have presented a many-body BSE study of low-lying excitons in PSII-RC with explicit protein environment using the TDHF@v_W method. Treating the reaction center and its surrounding protein environment on an equal quantum-mechanical footing reveals that the local electrostatic environment does not merely shift excitation energies,

but fundamentally reshapes the nature of the excited states. At the *ab initio* level, we show that protein embedding modifies excited states in a polarization-dependent way that alters transition-density character and exciton (de)localization.

We recover the lateral and transverse asymmetries reported in previous studies,[10,14] including D1 lateral branching for the second low-lying state. However, rather than viewing these effects purely as site-energy shifts of individual pigments, our results show that the excited states are inherently multi-pigment and not well captured by a localized picture. A fully quantum, multi-chromophore treatment yields delocalized excitons whose character reflects the collective electronic structure of the complex. The stochastic real-space framework imposes no localization at any stage, so this delocalization emerges naturally.

There is ongoing interest in better understanding the nature of the low-lying charge-transfer (CT) exciton in the PSII-RC. In the present TDHF@v_W calculations, we do not observe a distinct low-energy CT exciton; the low-lying states remain predominantly Frenkel-like. Previous qpGW-BSE calculations on the full chromophoric PSII-RC[26] without explicit environmental electrostatics also do not yield a low-lying CT exciton. This confirms that protein conformational dynamics plays a key role in stabilizing and accessing far-red CT states, as earlier suggested by QM/MM studies.[9]

Future Directions

We have shown that for large supramolecular systems the BSE does not become more intractable, but rather simpler: atomistic interactions self-average, screening becomes polarization-dominated, and stochastic techniques make fully quantum many-body treatment of biological nanostructures possible. Given the demonstrated scalability and accuracy of the present TDHF@v_W framework, several future directions follow:

First, the participation ratio analysis of the excited states indicates that even in very large PSII-RC models only a few tens of occupied-to-virtual transitions (in both isolated and embedded clusters) contribute appreciably to a particular excitation ω. The expansion

coefficients, cheaply obtained through the iterative Chebyshev expansion, will enable us to form a minimal exciton basis for effective excitonic models, which will be useful when combined with recent diabatization schemes developed for condensed-phase mixed QM/MM approaches that employ MBPT.[38]

A second direction would extend the TDHF@v_W framework beyond the static approximation by incorporating time-dependent screening. Using a frequency-dependent screened Coulomb interaction, $W(r, r', \omega)$, or a stochastically fitted translationally invariant form, $v_W(r - r', \omega)$, within a minimal exciton basis, would capture memory effects associated with the buildup of the electron-hole screening cloud. This would clarify how screening and environmental response influence exciton dissipation, redistribution, and the possible emergence of CT excitons in very large biological complexes.[36,39,40]

Third, future work will use the present BSE framework to assess the effects of mutating nearby amino-acid residues. The PSII-RC exhibits residue-dependent spectral shifts that can be probed by mutating nearby amino-acid residues. This will be analogous to TDDFT mutation studies done earlier with TD-CAM-B3LYP.[14] Coupling the method with molecular dynamics will enable a more realistic treatment of environmental fluctuations, extending the framework toward predictive excitonic structure and dynamics in complex nanoscale photosynthetic systems.

Methods

Computational Details

Ground-state simulations were performed within a plane-wave pseudopotential DFT framework using Troullier–Martins norm-conserving pseudopotentials[41] and the LDA exchange–correlation functional.[42] The mean-field electronic structure was then refined using the near-gap RSH-DFT approach[34] with the CAM-LDA0 functional.[16] For these conjugated supramolecular systems, the resulting orbital energies provide an accurate starting point for excitonic cal-

culations, and no additional GW quasiparticle correction was applied.

Excited states were computed using the TDHF@v_W framework,[28] which is formally equivalent to the static BSE but avoids constructing the screened Coulomb matrix explicitly. Instead, the screened interaction is represented by a translationally invariant kernel, $v_W(r-r')$, obtained from a stochastic fitting procedure. The action of the screened Coulomb operator on randomly sampled occupied–occupied pair densities is evaluated through short-time stochastic time-dependent Hartree propagation.[29,30,34,43] This captures the full k-dependent polarization response of the system without building or storing the dielectric matrix.

Exchange integrals in both the RSH-DFT stage and the linear-response calculations were evaluated using our mixed deterministic and sparse-stochastic compression of the plane-wave kernels.[27,30,34] Long-wavelength components were treated deterministically, while the high-k space was represented by a compact sparse-stochastic auxiliary basis. In practice, this reduces millions of reciprocal vectors to on the order of 10^4 separable terms at the same level of accuracy.

Optical spectra and frequency-resolved exciton amplitudes were obtained using an iterative Chebyshev expansion of the full two-particle Liouvillian,[27,28] including resonant-antiresonant coupling beyond the Tamm-Dancoff approximation. This avoids explicit diagonalization of the excitonic Hamiltonian and enables fully quantum-mechanical simulations of biomolecular systems containing several thousand valence electrons. The resulting exciton amplitudes are used to construct the transition-densities provided in the Results section.

Further numerical details and convergence tests are provided in the SI.

Acknowledgments

We are grateful to Justin R. Caram for useful discussions. This work is supported by the National Science Foundation (NSF) under Grant No. CHE-2245253. Computational resources were provided by the Expanse Cluster at the San Diego Supercomputer Center through allo-

cations PHY250047, PHY240131, and CHE240067, under the Advanced Cyberinfrastructure Coordination Ecosystem: Services & Support (ACCESS) program.

Supporting Information Available

The Supporting Information (SI) includes: methodology; workflow for PSII-RC geometry extraction; basis-set extrapolation of optical spectra; dominant transitions for isolated and protein-embedded PSII-RC; frontier molecular orbitals; parameterized results for the inverse dielectric function $\epsilon^{-1}(k)$; full vs. TDA TDHF@v_w spectra. Cartesian coordinate files (in Å) for the isolated and protein-embedded PSII-RC are provided as `psiirc_isolated.xyz` and `psiirc_embedded.xyz`.

References

1. Nelson, N.; Ben-Shem, A. The complex architecture of oxygenic photosynthesis. *Nature Reviews Molecular Cell Biology* **2004**, *5*, 971–982.

2. Stirbet, A.; Lazár, D.; Guo, Y.; Govindjee, G. Photosynthesis: basics, history and modelling. *Annals of Botany* **2020**, *126*, 511–537.

3. Umena, Y.; Kawakami, K.; Shen, J. R.; Kamiya, N. Crystal structure of oxygen-evolving photosystem II at a resolution of 1.9Å. *Nature* **2011**, *473*, 55–60.

4. Nocera, D. G. The Artificial Leaf. *Accounts of Chemical Research* **2012**, *45*, 767–776.

5. Brédas, J.-L.; Sargent, E. H.; Scholes, G. D. Photovoltaic concepts inspired by coherence effects in photosynthetic systems. *Nature Materials* **2017**, *16*, 35–44.

6. Renger, T.; Marcus, R. A. On the relation of protein dynamics and exciton relaxation in pigment–protein complexes: An estimation of the spectral density and a theory for the calculation of optical spectra. *The Journal of Chemical Physics* **2002**, *116*, 9997–10019.

7. Novoderezhkin, V. I.; Van Grondelle, R. Physical origins and models of energy transfer in photosynthetic light-harvesting. *Physical Chemistry Chemical Physics* **2010**, *12*, 7352.

8. Sirohiwal, A.; Neese, F.; Pantazis, D. A. Protein Matrix Control of Reaction Center Excitation in Photosystem II. *Journal of the American Chemical Society* **2020**, *142*, 18174–18190.

9. Sirohiwal, A.; Pantazis, D. A. The Electronic Origin of Far-Red-Light-Driven Oxygenic Photosynthesis. *Angewandte Chemie International Edition* **2022**, *61*, e202200356.

10. Sirohiwal, A.; Pantazis, D. A. Reaction Center Excitation in Photosystem II: From Multiscale Modeling to Functional Principles. *Accounts of Chemical Research* **2023**, *56*, 2921–2932.

11. Köse, M.; Khatri, R.; Dunietz, B. Dielectric Anisotropy Mitigated by Hydrogen Bonding Governs the Driving Force of Charge Transport within Quinone Pairs in Photosynthetic Reaction Centers. *The Journal of Physical Chemistry. A* **2025**, *129*.

12. Müh, F.; Plöckinger, M.; Renger, T. Electrostatic Asymmetry in the Reaction Center of Photosystem II. *The Journal of Physical Chemistry Letters* **2017**, *8*, 850–858.

13. Frankcombe, T. J. Explicit calculation of the excited electronic states of the Photosystem II Reaction Centre. *Physical Chemistry Chemical Physics* **2015**, *17*, 3295–3302.

14. Kavanagh, M. A.; Karlsson, J. K. G.; Colburn, J. D.; Barter, L. M. C.; Gould, I. R. A TDDFT investigation of the Photosystem II reaction center: Insights into the precursors to charge separation. *Proceedings of the National Academy of Sciences* **2020**, *117*, 19705–19712.

15. Dreuw, A.; Head-Gordon, M. Failure of Time-Dependent Density Functional Theory for Long-Range Charge-Transfer Excited States: The Zincbacteriochlorin-Bacteriochlorin

and Bacteriochlorophyll-Spheroidene Complexes. *Journal of the American Chemical Society* **2004**, *126*, 4007–4016.

16. Yanai, T.; Tew, D. P.; Handy, N. C. A new hybrid exchange–correlation functional using the Coulomb-attenuating method (CAM-B3LYP). *Chemical Physics Letters* **2004**, *393*, 51–57.

17. Baer, R.; Livshits, E.; Salzner, U. Tuned Range-Separated Hybrids in Density Functional Theory. *Annual Review of Physical Chemistry* **2010**, *61*, 85–109.

18. Stein, T.; Kronik, L.; Baer, R. Reliable Prediction of Charge Transfer Excitations in Molecular Complexes Using Time-Dependent Density Functional Theory. *Journal of the American Chemical Society* **2009**, *131*, 2818–2820.

19. Stein, T.; Eisenberg, H.; Kronik, L.; Baer, R. Fundamental Gaps in Finite Systems from Eigenvalues of a Generalized Kohn-Sham Method. *Phys. Rev. Lett.* **2010**, *105*, 266802.

20. Mandal, A.; Herbert, J. M. Simplified Tuning of Long-Range Corrected Time-Dependent Density Functional Theory. *The Journal of Physical Chemistry Letters* **2025**, *16*, 2672–2680.

21. Strinati, G. Application of the Green's functions method to the study of the optical properties of semiconductors. *La Rivista del Nuovo Cimento* **1988**, *11*, 1–86.

22. Rohlfing, M.; Louie, S. G. Electron-hole excitations and optical spectra from first principles. *Phys. Rev. B* **2000**, *62*, 4927–4944.

23. Blase, X.; Duchemin, I.; Jacquemin, D.; Loos, P.-F. The Bethe–Salpeter Equation Formalism: From Physics to Chemistry. *The Journal of Physical Chemistry Letters* **2020**, *11*, 7371–7382.

24. Hashemi, Z.; Leppert, L. Assessment of the *Ab Initio* Bethe–Salpeter Equation Approach

for the Low-Lying Excitation Energies of Bacteriochlorophylls and Chlorophylls. *The Journal of Physical Chemistry A* **2021**, *125*, 2163–2172.

25. Li, J.; Olevano, V. Bethe-Salpeter equation insights into the photo-absorption function and exciton structure of chlorophyll a and b in light-harvesting complex II. *Journal of Photochemistry and Photobiology B: Biology* **2022**, *232*, 112475.

26. Förster, A.; Visscher, L. Quasiparticle Self-Consistent GW-Bethe–Salpeter Equation Calculations for Large Chromophoric Systems. *Journal of Chemical Theory and Computation* **2022**, *18*, 6779–6793.

27. Sereda, M.; Allen, T.; Bradbury, N. C.; Ibrahim, K. Z.; Neuhauser, D. Sparse-Stochastic Fragmented Exchange for Large-Scale Hybrid Time-Dependent Density Functional Theory Calculations. *Journal of Chemical Theory and Computation* **2024**, *20*, 4196–4204.

28. Bradbury, N. C.; Li, B. Y.; Allen, T.; Caram, J. R.; Neuhauser, D. No more gap-shifting: Stochastic many-body-theory based TDHF for accurate theory of polymethine cyanine dyes. *The Journal of Chemical Physics* **2024**, *161*, 141101.

29. Neuhauser, D.; Gao, Y.; Arntsen, C.; Karshenas, C.; Rabani, E.; Baer, R. Breaking the Theoretical Scaling Limit for Predicting Quasiparticle Energies: The Stochastic GW Approach. *Physical Review Letters* **2014**, *113*, 076402.

30. Vlček, V.; Li, W.; Baer, R.; Rabani, E.; Neuhauser, D. Swift GW beyond 10,000 electrons using sparse stochastic compression. *Physical Review B* **2018**, *98*, 075107.

31. Allen, T.; Nguyen, M.; Neuhauser, D. GW with hybrid functionals for large molecular systems. *The Journal of Chemical Physics* **2024**, *161*, 114116.

32. Sharma, S.; Dewhurst, J. K.; Sanna, A.; Gross, E. K. U. Bootstrap Approximation for the Exchange-Correlation Kernel of Time-Dependent Density-Functional Theory. *Physical Review Letters* **2011**, *107*.

33. Li, B. Y.; Duong, T.; Allen, T.; Bradbury, N. C.; Caram, J. R.; Neuhauser, D. Parameterized attenuated exchange for generalized TDHF@v_W applications. *The Journal of Chemical Physics* **2025**, *163*, 034102.

34. Bradbury, N. C.; Allen, T.; Nguyen, M.; Neuhauser, D. Deterministic/Fragmented-Stochastic Exchange for Large-Scale Hybrid DFT Calculations. *Journal of Chemical Theory and Computation* **2023**, *19*, 9239–9247.

35. Allen, T.; Li, B. Y.; Duong, T.; Williams, K.; Neuhauser, D. Efficient plane-wave approach to generalized Kohn-Sham density functional theory of solids with mixed deterministic and stochastic exchange. *Phys. Rev. B* **2025**, *112*, 155104.

36. Ma, Y.; Rohlfing, M.; Molteni, C. Excited states of biological chromophores studied using many-body perturbation theory: Effects of resonant-antiresonant coupling and dynamical screening. *Phys. Rev. B* **2009**, *80*, 241405.

37. Martyna, G. J.; Tuckerman, M. E. A reciprocal space based method for treating long range interactions in ab initio and force-field-based calculations in clusters. *The Journal of Chemical Physics* **1999**, *110*, 2810–2821.

38. Rodriguez-Mayorga, M.; Blase, X.; Duchemin, I.; D'Avino, G. From Many-Body *Ab Initio* to Effective Excitonic Models: A Versatile Mapping Approach Including Environmental Embedding Effects. *Journal of Chemical Theory and Computation* **2024**, *20*, 8675–8688.

39. Rebolini, E.; Toulouse, J. Range-separated time-dependent density-functional theory with a frequency-dependent second-order Bethe-Salpeter correlation kernel. *The Journal of Chemical Physics* **2016**, *144*, 094107.

40. Loos, P.-F.; Blase, X. Dynamical correction to the Bethe-Salpeter equation beyond the plasmon-pole approximation. *The Journal of Chemical Physics* **2020**, *153*, 114120.

41. Troullier, N.; Martins, J. L. Efficient pseudopotentials for plane-wave calculations. *Phys. Rev. B* **1991**, *43*, 1993–2006.

42. Perdew, J. P.; Wang, Y. Accurate and simple analytic representation of the electron-gas correlation energy. *Phys. Rev. B* **1992**, *45*, 13244–13249.

43. Bradbury, N. C.; Nguyen, M.; Caram, J. R.; Neuhauser, D. Bethe–Salpeter equation spectra for very large systems. *The Journal of Chemical Physics* **2022**, *157*, 031104.

TOC Graphic

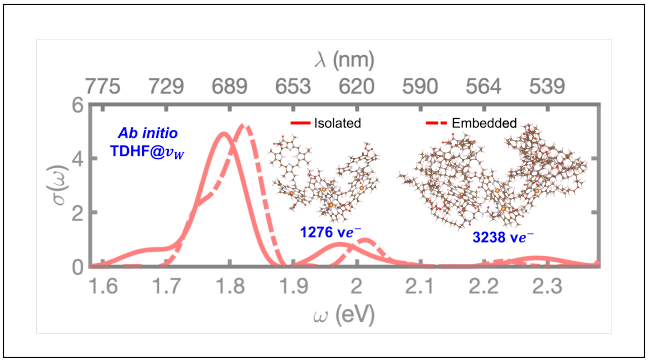
λ (nm)
775 729 689 653 620 590 564 539
6
4
2
0
σ(ω)
Ab initio
TDHF@v_W
Isolated
Embedded
1276 ve⁻
3238 ve⁻
1.6 1.7 1.8 1.9 2 2.1 2.2 2.3
ω (eV)

Supporting Information: Environment-Induced Exciton Renormalization in the Photosystem II Reaction Center

Tucker Allen,*,† Barry Y. Li,† Nadine C. Bradbury,‡ and Daniel Neuhauser†

†*Department of Chemistry and Biochemistry, University of California, Los Angeles, Los Angeles, CA, 90095, USA*

‡*Department of Chemistry, Princeton University, Princeton, NJ, 08544, USA*

E-mail: tuckerallen27@ucla.edu

Date: February 23, 2026

I. Methodology

We summarize here the key ingredients to the TDHF@v_W method that enable a large-scale comparative study of the isolated and protein-embedded PSII-RC. In Section A, we describe the mixed deterministic/sparse-stochastic approach to efficiently evaluate exchange integrals within a plane-wave representation. In Section B, we briefly discuss how the anisotropic response kernel v_W is generated through short-time stochastic time-dependent Hartree (TDH) dynamics. In Section C, we outline how to obtain the linear-response optical absorption cross-section and exciton amplitudes through an iterative Chebyshev polynomial expansion of spectral operators.

A. Mixed Deterministic and Stochastic Evaluation of Exchange Integrals

In this section, we explain the stochastic-fragmented approach, which is a key ingredient in our method. It allows the calculation of accurate exchange interactions with little numerical effort, by replacing the millions of explicit k-vector calculations with around $10,000-15,000$ "fragments", which are each quite easy to act on.

Within a plane-wave grid-based approach, generation of exchange integrals is costly due to many basis elements. Here we discuss a mixed deterministic/sparse-stochastic approach, developed in Refs.[1–3] and applied in Refs.[4–7] First, given a general exchange interaction kernel, $u(k)$, where k denotes a reciprocal lattice vector, we divide the kernel between a few long-wavelength, low-k components that are evaluated deterministically, and the remainder high-k terms are treated through a sparse-stochastic basis that is system-size independent, yet describes the full exchange interaction.

To achieve this fragmentation of $u(k)$, the following resolution-of-the-identity is introduced:

$$I = \sum_{k_{\text{low}}} |k_{\text{low}}\rangle \langle k_{\text{low}}| + \sum_{k_{\text{high}}} |k_{\text{high}}\rangle \langle k_{\text{high}}| . \tag{1}$$

In this basis a general interaction becomes:

$$\begin{aligned} u(k) = &\sum_{k_{\text{low}}} |k_{\text{low}}\rangle u(k_{\text{low}}) \langle k_{\text{low}}| \\ &+ \sum_{k_{\text{high}}} \sqrt{|u(k_{\text{high}})|} |k_{\text{high}}\rangle \langle k_{\text{high}}| \sqrt{|u(k_{\text{high}})|}. \end{aligned} \tag{2}$$

The key ingredient is then that the high-k space is compressed by using short, "fragmented", random vectors:

$$\alpha(k_{\text{high}}) = \pm\sqrt{\frac{N_{k_{\text{high}}}}{L}} A_\alpha(k_{\text{high}}), \tag{3}$$

where $N_{k_{\text{high}}}$ is the number of high-k terms being sampled, L is the length of each fragment,

and $A_\alpha(k_{\text{high}}) = \pm 1$ for k_{high} within the length-L fragment, and 0 outside the fragment. The length L is much smaller than the extent of the k_{high}-grid, enabling a large number of fragments to sample efficiently the k_{high}-space. The high-k contribution to $u(k)$ is now a set of N_α states, $\{|\zeta\rangle\}$, with components

$$\langle k_{\text{high}}|\zeta\rangle = \sqrt{|u(k_{\text{high}})|}\ \alpha(k_{\text{high}}). \tag{4}$$

The full auxiliary basis, $N_\xi = N_{k_{\text{low}}} + N_\alpha$, is then

$$|\xi\rangle = \{\sqrt{|u(k_{\text{low}})\,|}\ |k_{\text{low}}\rangle\} \oplus \{|\zeta\rangle\}, \tag{5}$$

and the interaction is now a sum over separable terms:

$$u = \sum_\xi |\xi\rangle\langle\xi|. \tag{6}$$

This approach to evaluating exchange integrals is implemented both in the ground-state RSH-DFT stage, using the near-gap hybrid DFT method (detailed in[2]), and the linear-response TDHF@v_W spectral simulations, detailed in.[4] In the present study, the sparse-stochastic basis consists of $N_\alpha = 5,000$ vectors and the total number of $|\xi\rangle$ terms is then between $10,000 - 15,000$. For comparison, a fully deterministic calculation would involve $N_k = 17,808,384$ and $38,223,360$ plane waves for the isolated and protein-embedded PSII-RC, respectively. The mixed deterministic/sparse-stochastic basis therefore corresponds to less than 0.1% of the deterministic plane-wave basis-set size.

B. Stochastic Fitting of Screened Coulomb Operator W

To describe dielectric screening in large biological systems at the random-phase approximation (RPA) level, we evaluate the action of the screened Coulomb operator W on stochastic occupied-occupied pair densities using stochastic TDH propagation. Technical details are

given in Refs.;[8,9] here we focus on the stochastic fitting procedure used to construct the screened-exchange kernel v_W. The $v_W(r-r')$ potential masks atomic details but was found by us to be very accurate for large systems as it gives the overall k-dependent polarization.

An optimal fit of v_W to W is derived by minimizing the following objective:[10]

$$J = \sum_{ij} (\phi_i \phi_j | (W - v_W)^2 | \phi_i \phi_j), \tag{7}$$

where $\{\phi_i\}$ are a set of mean-field occupied molecular orbitals (MOs), obtained from a prior RSH-DFT calculation. Next, we replace the deterministic occupied-occupied MO products with a stochastic realization. We define a stochastic process, and two independent stochastic vectors,

$$\begin{aligned} \bar{\beta}(r) &= \sum_l \bar{\beta}_l \phi_l(r), \\ \bar{\bar{\beta}}(r) &= \sum_l \bar{\bar{\beta}}_l \phi_l(r), \end{aligned} \tag{8}$$

where the sums extend over occupied states and $\bar{\beta}_l = \pm 1$, $\bar{\bar{\beta}}_l = \pm 1$. Using the identity $\left\{\bar{\beta}_i \bar{\beta}_j\right\} = \left\{\bar{\bar{\beta}}_i \bar{\bar{\beta}}_j\right\} = \delta_{ij}$, where curly brackets denote an average over many stochastic instances, it follows that

$$\left\{\bar{\beta}_i \bar{\bar{\beta}}_j \beta(r)\right\} = \phi_i(r)\phi_j(r), \tag{9}$$

where $\beta(r) \equiv \bar{\beta}(r)\bar{\bar{\beta}}(r)$. Upon replacement of the deterministic pair-densities with $\beta(r)$ and moving to reciprocal space, it can be shown that:

$$v_W(k) = \left\{ \frac{\beta^*(k) \langle k|W|\beta\rangle}{|\langle k|\beta\rangle|^2} \right\}_\beta, \tag{10}$$

where $\beta(k)$ is the momentum-space representation of a random occupied-occupied pair density. The action $\langle k|W|\beta\rangle$ is first calculated in real-space, with a short-time stochastic TDH propagation. For further technical details on the real-time dynamics, we refer to Refs.[5,11]

For the respective isolated and protein-embedded PSII-RC systems, the stochastic fit captures 76.8% and 84.3% of the overall screened interaction W. The residual, $\langle (W - v_W)^2 \rangle / \langle W^2 \rangle$, decreases from 23.2% to 15.7% upon protein embedding, indicating that the translationally invariant representation becomes more accurate in the larger system.

C. Iterative Chebyshev Approach to Optical Spectra and Exciton Amplitudes

We compute optical spectra and frequency-resolved exciton amplitudes using an iterative Chebyshev polynomial expansion of the full TDHF@v_W Liouvillian. The full Liouvillian satisfies the following eigenvalue problem:[12]

$$\mathcal{L} \begin{pmatrix} f^+ \\ f^- \end{pmatrix} = \hbar\omega \begin{pmatrix} 1 & 0 \\ 0 & -1 \end{pmatrix} \begin{pmatrix} f^+ \\ f^- \end{pmatrix} \tag{11}$$

where the two-particle Liouvillian is expressed as a block matrix:

$$\mathcal{L} = \begin{pmatrix} A & B \\ -B & -A \end{pmatrix}, \tag{12}$$

and f^+, f^- are the positive- and negative-frequency transition eigenvectors, respectively. For spin-singlet excitons, the A and B matrices are:

$$\begin{aligned} A_{ia,jb} &= (\varepsilon_a - \varepsilon_i)\delta_{ij}\delta_{ab} + 2(ia|jb) - (\phi_a\phi_b|v_W|\phi_i\phi_j) \\ B_{ia,bj} &= 2(ia|bj) - (\phi_a\phi_j|v_W|\phi_i\phi_b), \end{aligned} \tag{13}$$

where the electron repulsion integrals are:

$$(ia|jb) = \int \phi_i(r)\phi_a(r)|r - r'|^{-1}\phi_j(r')\phi_b(r')dr'dr, \tag{14}$$

and $(ia|jb)$=$(ia|bj)$. The screened exchange integrals for the diagonal portion of $\mathcal{L}$ are:

$$(\phi_a\phi_b|v_W|\phi_i\phi_j) = \int \phi_a(r)\phi_b(r)v_W(r-r')\phi_i(r')\phi_j(r')dr'dr, \tag{15}$$

with analogous elements for the off-diagonal coupling part. We have introduced valence $\varepsilon_{i,j,\ldots}$ (occupied) and conduction $\varepsilon_{a,b,\ldots}$ (virtual) energies and associated real-valued orbitals from a preceding RSH-DFT calculation. In this work, we use the CAM-LDA0 hybrid functional,[13] with hybrid-exchange parameters: $\alpha = 0.19, \beta = 0.46, \gamma = 0.33$ Bohr^{-1}.

To iteratively solve for the excitation energies and associated amplitudes of $\mathcal{L}$, we define an initial exciton vector (assuming laser polarization in the x-direction for simplicity):

$$|\chi_{ia}\rangle = \begin{pmatrix} f_{ia}^{+} \\ f_{ia}^{-} \end{pmatrix} = \begin{pmatrix} +\langle\phi_a|x|\phi_i\rangle \\ -\langle\phi_a|x|\phi_i\rangle \end{pmatrix}. \tag{16}$$

Then, the absorption cross-section is obtained via

$$\sigma(\omega) \propto \omega\langle\chi_{ia}|\delta(\mathcal{L}-\omega)|\chi_{ia}\rangle, \tag{17}$$

where one evaluates the delta function by finding the Chebyshev residues:

$$R_n^{\pm} = \sum_{ia}\langle f_{ia}^{\pm}|T_n(\tilde{\mathcal{L}})|f_{ia}^{\pm}\rangle, \tag{18}$$

with $T_n(\tilde{\mathcal{L}})$ being the n-th Chebyshev polynomial, and $\tilde{\mathcal{L}}$ the scaled Liouvillian with eigenvalues between the interval $[-1,+1]$. For numerical details on the matrix-vector applications, we refer to Ref.[4] One then can write the correlation function as:

$$\sigma(\omega) = \sum_{n=0}^{N_{\text{Cheb}}} c_n(\omega)(R_n^{+} + R_n^{-}), \tag{19}$$

where $c_n(\omega)$ are smoothly-decaying numerical coefficients[14] and the Chebyshev length, N_{Cheb},

is set to 2000 terms. This value for N_{Cheb} results in a peak broadening of roughly 0.1 eV for absorption spectra.

In addition to the Chebyshev residues used to construct $\sigma(\omega)$, the same recursion yields frequency-resolved exciton amplitudes at essentially no additional cost. During the Chebyshev propagation we generate the vectors $|u_n\rangle \equiv T_n(\tilde{\mathcal{L}})|\chi\rangle$ for $n = 0, \ldots, N_{\mathrm{Cheb}}$. For sampling a specific frequency ω, a filtered exciton vector is then obtained as $|f(\omega)\rangle \equiv \delta(\mathcal{L} - \omega)|\chi\rangle \approx \sum_{n=0}^{N_{\mathrm{Cheb}}} c_n(\omega)|u_n\rangle$, using the same Chebyshev coefficients $c_n(\omega)$ used for the absorption cross-section. The components $f_{ia}^{\pm}(\omega)$ provide the exciton transition amplitudes in the valence-conduction basis and are normalized such that $\sum_{ia} |f_{ia}(\omega)|^2 = 1$.

From the normalized amplitudes we define the real-space transition density $\rho(r;\omega) = \sum_{ia}[f_{ia}^{+}(\omega) + f_{ia}^{-}(\omega)]\phi_i(r)\phi_a(r)$. Exciton delocalization is quantified via the participation ratio, $\mathrm{PR}(\omega) = 1/\sum_{ia} |f_{ia}(\omega)|^4$.

II. Workflow of PSII-RC Geometry Extraction

The structural model of the PSII-RC, based on chlorophyll-a (CLA) and its surrounding protein environment, is derived from an experimentally resolved PSII crystal structure reported in Ref.[15] Starting from the full biological PDB, all CLA residues associated with the hexameric pigment site are identified,[15] and a local protein environment is extracted using a radial cutoff that retains only residues in direct spatial proximity to the pigments. This procedure preserves the native relative positions and orientations of the chromophores while reducing the system size to a computationally tractable cluster.

The resulting coordinates are further processed to ensure chemical completeness, including fragment cleanup and hydrogen addition. For the multi-chlorin system, we employ a QM-optimized structure in which the internal geometries of the pigment macrocycles are replaced by high-level QM-optimized structures taken from prior reference calculations by Förster and Visscher,[16] while preserving their positions within the protein scaffold. The re-

maining protein environment is subsequently relaxed using the extended tight-binding force-field approach (xTBFF) as implemented in the ORCA 6.0 package,[17,18] with the pigment "core" held fixed.

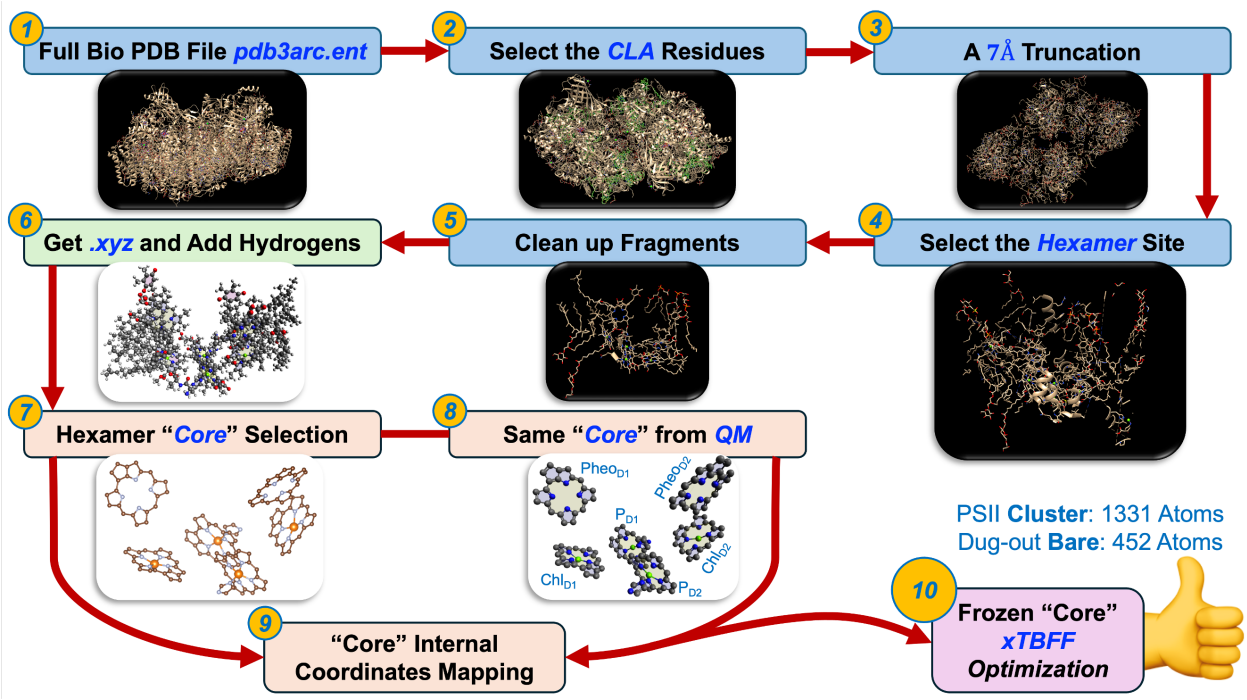

Figure 1: Schematic workflow for constructing the isolated and protein-embedded PSII-RC from the full experimental PDB structure, including pigment selection, protein truncation, core replacement with quantum-optimized geometries, and environment relaxation using xTBFF with a frozen pigment core.

Fig. 1 summarizes the construction and preparation of a protein-embedded Photosystem II reaction center (PSII-RC). Starting from a full experimental PDB structure, the workflow isolates the relevant pigment-protein region, reduces the system size through spatial truncation, enforces chemical consistency, and finally combines high-level quantum-optimized pigment geometries with a low-cost force-field relaxation of the environment using xTBFF,[17] while keeping the chromophore core frozen. The detailed workflow is listed below:

- **Step 1: Biological PDB structure.** The workflow begins from the experimentally resolved PSII structure (`pdb3arc.ent`) from Ref.[15] and its online Data Deposits. This file contains the complete protein complex, cofactors, pigments, and associated

residues, represented in crystallographic coordinates. At this stage, the system is chemically heterogeneous, extremely large ($\sim 55,000$ atoms), and not directly suitable for quantum calculations.

- **Step 2: Selection of CLA (chlorophyll-a) residues.** From the full PDB, all CLA residues corresponding to chlorophyll-a pigments are identified and selected. This step isolates the electronic subsystem of interest while preserving the original pigment positions and orientations relative to the protein scaffold.

- **Step 3: Spatial truncation (7-Å cutoff).** A 7-Å radial truncation is applied around the selected CLA pigments. All protein residues and cofactors with at least one atom within this cutoff are retained, while the remainder of the PSII complex is removed. This step reduces the system size while preserving the local electrostatic and steric environment that directly influences pigment geometry and electronic structure. The truncation is purely geometric and does not yet enforce chemical capping or saturation.

- **Step 4: Selection of the hexamer site.** From the truncated region, the specific chlorophyll hexamer site is selected. This hexamer corresponds to the functionally relevant pigment cluster responsible for excitonic and charge-transfer processes in PSII. The surrounding protein residues retained at this stage provide an explicit, local environment for the pigments, resulting in a mixed pigment-protein cluster.

- **Step 5: Fragment cleanup and chemical repair.** Truncation inevitably breaks covalent bonds within protein residues. In this step, all dangling bonds are identified, fragmented residues are capped or repaired, and obvious steric clashes and crystallographic artifacts are removed.

- **Step 6: XYZ generation and hydrogen addition.** The cleaned protein-embedded PSII-RC is converted from PDB to XYZ format. Hydrogen atoms are added to all other

atoms according to standard valence rules, yielding a chemically complete structure. At this point, the protein-embedded PSII-RC contains 1331 atoms, including pigments, protein residues, and hydrogens.

- **Step 7: Definition of the hexamer "core".** A core region of 186 atoms is defined, consisting exclusively of the chlorophyll macrocycles and their central Mg atoms (and 2 directly bonded substituents). This core represents the electronic subsystem to be treated at high quantum-chemical accuracy.

- **Step 8: Replacement with a high-level QM-optimized "core".** The geometries of the 186-atom chlorophyll core are replaced by high-level QM-optimized structures taken from an independent Ref.[19] This step ensures that the internal bond lengths, angles, and macrocycle planarity of each chlorophyll are described at a reliable quantum level; errors introduced by force-field or low-level optimization of the pigments are eliminated. The chromophore labeling in Fig. 1 follows the convention of Ref.[20]

- **Step 9: Internal coordinate mapping.** After replacement, a one-to-one mapping of internal coordinates is carried out between the original and substituted cores. This guarantees consistency of atom ordering, bonding topology, and connectivity between the pigment core and the surrounding environment. The mapping step is essential to avoid artificial strain or discontinuities at the pigment–protein boundary.

- **Step 10: xTBFF optimization with frozen "core".** Finally, the full protein-embedded PSII-RC is optimized using xTBFF (extended tight-binding force field),[17,18] while freezing all atoms in the 186-atom chlorophyll core. Only the protein environment and peripheral atoms are allowed to relax.

The extended tight-binding framework (xTB), interfaced with ORCA 6.0, is a semiempirical quantum method that solves a simplified electronic Schrödinger equation using parameters fitted to DFT reference data. As a result, xTB retains an explicit electronic struc-

ture description, including electron density, self-consistent atomic charges, and orbital energies, while naturally allowing for bond formation and bond breaking without predefined connectivity.[17,18] The xTB force-field mode (xTBFF) builds on this quantum-mechanical foundation while adopting a force-field-like representation for large-scale structural relaxation. Although xTBFF organizes interactions in terms of bond stretches, angle bends, and torsional terms, the associated parameters are not fixed but are dynamically derived from the underlying xTB electronic structure.[17] Electrostatic interactions are governed by self-consistent charges rather than predefined atom types. Consequently, xTBFF preserves chemically meaningful bonding information and environmental responsiveness that are absent in classical force fields, which rely on static atom types, fixed parameters, and manual reparameterization.[17] Both coordinate sets (in Å) are provided in the additional supporting materials as `psiirc_embedded.xyz` and `psiirc_isolated.xyz`.

III. Basis-set Extrapolation for Optical Spectra

The optical spectra provided in the main text use a transition space of $N_v = 200$ valence orbitals and $N_c = 400$ conduction orbitals to construct the two-particle Liouvillian. For both the isolated and embedded PSII-RC models, this exciton basis-set size is sufficient to converge the spectral shapes below 3 eV. We have confirmed that increasing N_c beyond 400 does not affect either the spectral shapes or peak positions for low-energy (< 3 eV) excitations. The consistent exciton basis-set size also allows us to directly compare the transition densities and participation ratios of each system.

We include a rigid shift in the reported spectra by performing a series of calculations for different N_v and N_c. Here, we perform a simple linear extrapolation to converge the absolute peak positions of spectra. Table 1 shows peak positions as a function of N_v, where we vary the number of valence orbitals while doubling the number of conduction orbitals for each selected N_v, i.e., $N_c = 2N_v$. This convention is arbitrary, and we have confirmed for both

systems that spectra are converged within 0.01 eV even when going beyond $N_c = 2N_v$ for all low-energy (< 3 eV) excitations.

Table 1: Onset absorption peak energies calculated using the TDHF@v_W method with different values of N_v and N_c for the isolated and protein-embedded PSII-RC at different polarization directions. Note that $N_c = 2N_v$ holds in all cases.

	N_v	N_c	**Isolated Peak (eV)**	**Embedded Peak (eV)**
x**-pol**	50	100	-	1.84
	100	200	1.79	1.82
	150	300	1.73	1.82
	200	400	1.71	1.79
	300	600	1.68	1.77
y**-pol**	50	100	-	1.90
	100	200	1.89	1.90
	150	300	1.87	1.87
	200	400	1.84	1.87
	300	600	1.82	1.84
	400	800	1.79	-
z**-pol**	50	100	-	1.84
	100	200	1.76	1.82
	150	300	1.73	1.82
	200	400	1.71	1.79
	300	600	1.68	1.79

The linear extrapolation is performed with the target function, $\omega = a(1/N_v) + b$, where ω is the onset absorption energy in eV, a and b are regression parameters. Table 2 shows the linear extrapolation results and the predicted peaks at $N_v \to N_v^{\max} = N_{\text{occ}}$.

Table 2: Results from linear extrapolation for the isolated and protein-embedded PSII-RC at different polarization directions.

System	Polarization	a	b	$N_v = N_v^{\max}$	**Peak at $N_v^{\max}$ (eV)**
Isolated	x-pol	16.3	1.63	638	**1.65**
	y-pol	12.6	1.77	638	**1.79**
	z-pol	11.7	1.65	638	**1.67**
Embedded	x-pol	7.54	1.75	1619	**1.76**
	y-pol	8.23	1.82	1619	**1.82**
	z-pol	5.14	1.77	1619	**1.78**

In addition to converging with respect to N_v, we also converge the number of low-k vectors, $N_{k_{\text{low}}}$, used to evaluate the screened exchange matrix elements entering $\mathcal{L}$. Ex-

change is evaluated in a plane-wave basis; in the fully deterministic limit this corresponds to $(2)^3 N_x N_y N_z$ reciprocal vectors, where the $(2)^3$ comes from doubling the real-space cell in each direction using the Martyna–Tuckerman construct to minimize grid-reflection effects.[21]

To check convergence of peaks (i)-(iv) in the main text, we increased $N_{k_{\mathrm{low}}}$ (with fixed $N_v = 100$, $N_c = 200$) from $4683 \rightarrow 37523$ for the isolated PSII-RC and from $10091 \rightarrow 41299$ for the embedded PSII-RC, and observed no discernible change in the y-polarized spectra; we therefore consider the results converged with respect to $N_{k_{\mathrm{low}}}$ at the values used in the main text. The total auxiliary basis is $N_\xi = N_{k_{\mathrm{low}}} + N_\alpha$, with $N_\alpha = 5000$ sparse vectors, giving a total of $10,000 - 15,000$ auxiliary vectors. A fully deterministic plane-wave calculation would require millions of basis elements; our approach achieves comparable accuracy with only thousands.

IV. Dominant Transitions in Isolated and Protein-embedded PSII-RC

This section lists the dominant valence-to-conduction orbital transition contributions for the low-energy excitations of the isolated and protein-embedded PSII-RC, along with the corresponding weights and participation ratios.

Table 3: Contributions of individual valence (VMO) and conduction (CMO) molecular orbitals to the first x-polarized excitation for the isolated PSII hexamer (Isolated) and the protein-embedded (Embedded) PSII-RC. The numbers in the VMO and CMO columns indicate the MO index relative to the HOMO (0) or LUMO (0). $|A|^2$ denotes the transition amplitude of each configuration (only dominant transitions with normalized $|A|^2 \geq 0.01$ are shown). PR denotes the participation ratio of the exciton, with larger values indicating contributions from a greater number of VMO to CMO transitions and increased exciton delocalization in the transition basis.

Isolated Peak 1 x-pol (1.66 eV)			**Embedded Peak 1 x-pol (1.75 eV)**		
VMO	CMO	$\|A\|^2$	VMO	CMO	$\|A\|^2$
0 (HOMO)	+5	0.029	0 (HOMO)	+5	0.019
−1	+6	0.046	0 (HOMO)	+7	0.015
−1	+11	0.333	0 (HOMO)	+12	0.027
−2	+11	0.061	−1	+5	0.064
−6	+9	0.016	−2	+2	0.122
−6	+11	0.377	−2	+10	0.016
−6	+16	0.035	−3	+5	0.021
−7	+17	0.017	−5	+5	0.023
−8	+11	0.018	−5	+12	0.044
			−7	0 (LUMO)	0.124
			−7	+6	0.118
			−9	+6	0.013
			−10	+2	0.015
			−10	+11	0.076
			−11	0 (LUMO)	0.144
			−11	+6	0.076
PR = 3.8			**PR = 11.7**		

Table 4: Molecular orbital transition analysis for the first y-polarized excited-state.

Isolated Peak 1 y-pol (1.79 eV)			**Embedded Peak 1 y-pol (1.82 eV)**		
VMO	CMO	$\|A\|^2$	VMO	CMO	$\|A\|^2$
0 (HOMO)	+4	0.018	0 (HOMO)	+5	0.028
0 (HOMO)	+5	0.091	0 (HOMO)	+7	0.174
−1	+5	0.143	−1	+7	0.018
−1	+11	0.106	−1	+13	0.112
−2	+5	0.012	−3	+7	0.041
−2	+11	0.061	−3	+13	0.094
−4	+5	0.011	−4	+3	0.201
−5	+5	0.063	−5	+3	0.010
−5	+11	0.034	−5	+7	0.024
−6	+3	0.036	−6	+4	0.016
−6	+9	0.043	−8	+9	0.014
−7	0 (LUMO)	0.068	−9	+3	0.019
−7	+6	0.021	−9	+11	0.141
−8	+3	0.061			
−8	+9	0.029			
−11	0 (LUMO)	0.028			
−11	+6	0.046			
PR = 15.3			**PR = 8.6**		

Table 5: Molecular orbital transition analysis for the first z-polarized excited-state.

Isolated Peak 1 z-pol (1.67 eV)			**Embedded Peak 1 z-pol (1.77 eV)**		
VMO	CMO	$\|A\|^2$	VMO	CMO	$\|A\|^2$
−3	+5	0.289	−1	+5	0.021
−3	+12	0.024	−2	+2	0.110
−4	+6	0.021	−2	+10	0.014
−4	+11	0.156	−5	+12	0.014
−5	+11	0.029	−7	0 (LUMO)	0.172
−8	+12	0.010	−7	+6	0.165
−9	+5	0.177	−9	+6	0.018
−9	+11	0.017	−10	+2	0.014
−10	+5	0.023	−10	+11	0.068
−10	+12	0.174	−11	0 (LUMO)	0.200
			−11	+6	0.106
PR = 5.8			**PR = 7.9**		

Table 6: Molecular orbital transition analysis for the x-polarized "hump" transition.

Isolated Hump x-pol (1.79 eV)			**Embedded Hump x-pol (1.83 eV)**		
VMO	CMO	$\|A\|^2$	VMO	CMO	$\|A\|^2$
0 (HOMO)	+5	0.054	0 (HOMO)	+7	0.035
−1	+5	0.079	−1	+13	0.021
−1	+11	0.056	−3	+3	0.012
−2	+11	0.034	−3	+13	0.018
−5	+3	0.011	−4	+3	0.433
−5	+5	0.033	−4	+11	0.023
−5	+9	0.013	−5	+3	0.020
−5	+11	0.019	−9	+3	0.042
−6	+3	0.158	−9	+11	0.296
−6	+9	0.151			
−8	+3	0.179			
−8	+9	0.105			
PR = 9.4			**PR = 3.6**		

Table 7: Molecular orbital transition analysis for the right shoulder ("hump") z-polarized excited state.

Isolated Hump z-pol (1.78 eV)			**Embedded Hump 1 z-pol (1.84 eV)**		
VMO	CMO	$\|A\|^2$	VMO	CMO	$\|A\|^2$
−4	0 (LUMO)	0.011	−3	+3	0.013
−5	0 (LUMO)	0.025	−4	+3	0.477
−7	0 (LUMO)	0.357	−4	+11	0.027
−7	+6	0.129	−5	+3	0.022
−9	0 (LUMO)	0.014	−9	+3	0.046
−9	+6	0.010	−9	+11	0.323
−11	0 (LUMO)	0.138			
−11	+2	0.010			
−11	+6	0.213			
PR = 4.8			**PR = 3.0**		

Table 8: Molecular orbital transition analysis for the second x-polarized excited state.

Isolated Peak 2 x-pol (2.01 eV)			**Embedded Peak 2 x-pol (2.02 eV)**		
VMO	CMO	$\|A\|^2$	VMO	CMO	$\|A\|^2$
-3	$+8$	0.048	-2	$+1$	0.077
-4	0 (LUMO)	0.017	-2	$+8$	0.044
-4	$+2$	0.338	-2	$+10$	0.329
-4	$+7$	0.038	-10	$+1$	0.416
-5	$+2$	0.063	-10	$+4$	0.031
-6	$+3$	0.012	-10	$+10$	0.024
-8	$+3$	0.011			
-9	$+2$	0.039			
-9	$+7$	0.251			
-10	$+1$	0.066			
-11	$+7$	0.011			
PR = 5.2			**PR = 3.4**		

Table 9: Molecular orbital transition analysis for the second y-polarized excited state.

Isolated Peak 2 y-pol (1.98 eV)			**Embedded Peak 2 y-pol (2.01 eV)**		
VMO	CMO	$\|A\|^2$	VMO	CMO	$\|A\|^2$
-3	$+1$	0.044	-2	$+2$	0.077
-3	$+8$	0.276	-2	$+9$	0.044
-4	$+2$	0.015	-2	$+11$	0.328
-6	$+3$	0.012	-10	$+2$	0.412
-6	$+9$	0.012	-10	$+5$	0.034
-7	0 (LUMO)	0.020	-10	$+11$	0.024
-7	$+6$	0.044			
-8	$+1$	0.018			
-8	$+3$	0.015			
-10	$+1$	0.378			
-10	$+8$	0.012			
-11	0 (LUMO)	0.046			
-11	$+6$	0.014			
PR = 4.4			**PR = 3.5**		

Table 10: Molecular orbital transition analysis for z-polarized excited state.

Isolated Peak 2 z-pol (1.99 eV)			**Embedded Peak 2 z-pol (2.04 eV)**		
VMO	CMO	$\|A\|^2$	VMO	CMO	$\|A\|^2$
-3	$+1$	0.039	-2	-2	0.078
-3	$+8$	0.247	-2	$+5$	0.045
-6	$+3$	0.048	-2	$+7$	0.334
-6	$+9$	0.029	-10	-2	0.421
-7	0 (LUMO)	0.016	-10	$+1$	0.035
-7	$+6$	0.033	-10	$+7$	0.025
-8	$+1$	0.030			
-8	$+3$	0.030			
-8	$+9$	0.041			
-10	$+1$	0.326			
-10	$+3$	0.013			
-10	$+8$	0.012			
-11	0 (LUMO)	0.037			
-11	$+6$	0.012			
PR = 5.6			**PR = 3.4**		

Table 11: Molecular orbital transition analysis for the third peak. Only the y-polarized data is shown as the spectra is isotropic for the isolated and protein-embedded PSII-RC individually.

Isolated Peak 3 y-pol (2.29 eV)			**Embedded Peak 3 y-pol (2.23 eV)**		
VMO	CMO	$\|A\|^2$	VMO	CMO	$\|A\|^2$
0 (HOMO)	0 (LUMO)	0.014	0 (HOMO)	$+5$	0.400
0 (HOMO)	$+5$	0.565	0 (HOMO)	$+7$	0.026
0 (HOMO)	$+10$	0.052	-1	$+5$	0.312
0 (HOMO)	$+11$	0.039	-1	$+12$	0.026
0 (HOMO)	$+16$	0.026	-1	$+13$	0.012
-1	$+4$	0.022	-3	$+5$	0.018
-1	$+5$	0.103	-5	$+5$	0.108
-1	$+11$	0.011	-6	$+5$	0.011
-2	$+4$	0.012			
-2	$+5$	0.052			
-5	$+5$	0.031			
PR = 3.0			**PR = 3.7**		

V. Frontier Molecular Orbitals

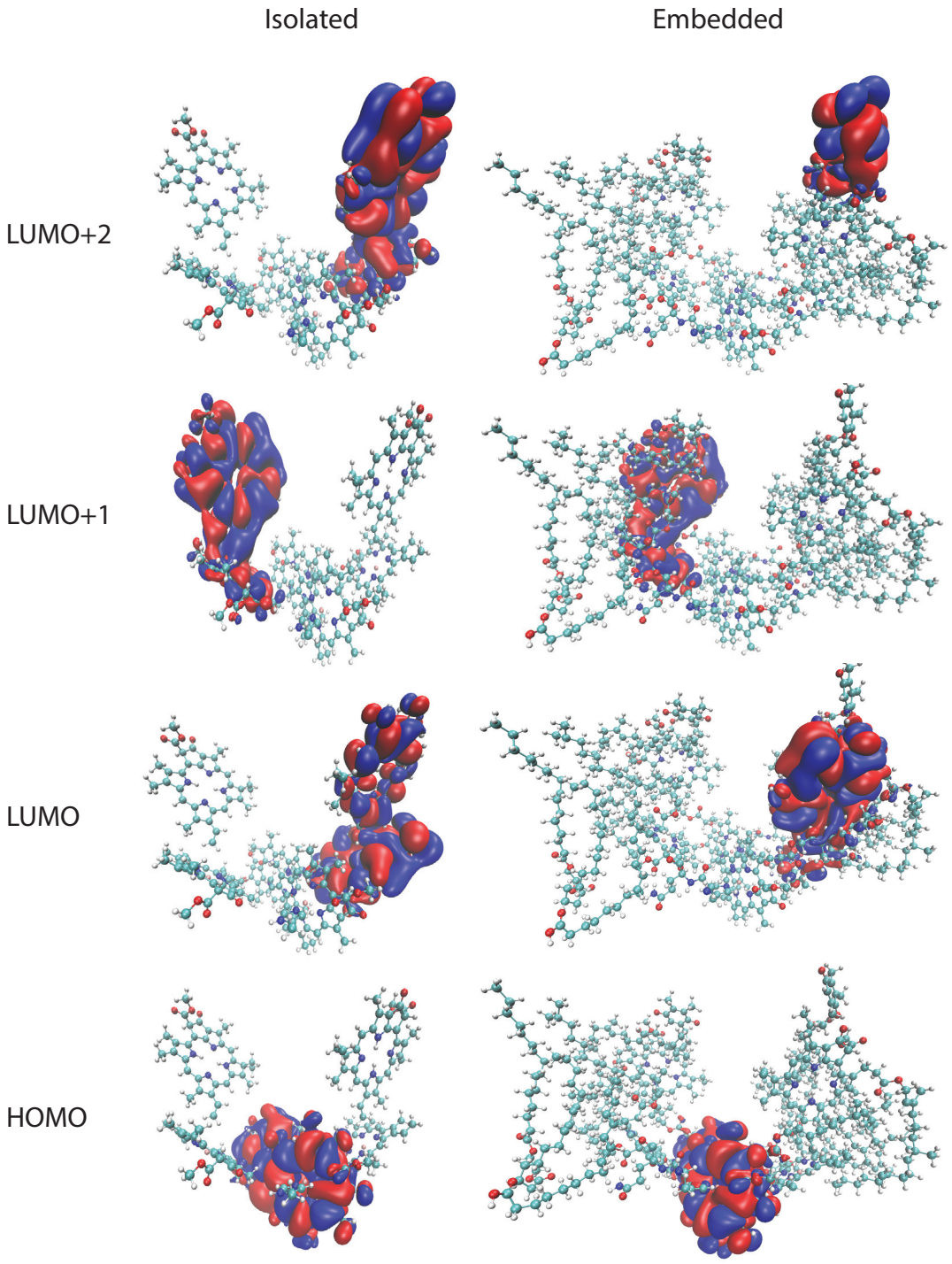

Figure 2: Molecular orbital plots for the isolated PSII-RC (left) and protein-embedded PSII-RC (right) using the CAM-LDA0 RSH functional. Isovalues of ± 0.002 Bohr$^{-3/2}$ are used for all orbitals with blue used for positive values and red for negative values.

The frontier molecular orbitals (MOs) for the isolated and protein-embedded PSII-RC systems are provided in Fig. 2. The CAM-LDA0 DFT bandgap for the isolated PSII-RC is 3.51 eV, and it decreases to 3.41 eV when the complex is placed in the protein environment. Overall, the environment has a stabilizing effect that pushes the single-particle spectrum to lower energies relative to the vacuum hexamer complex. The frontier orbitals remain predominantly chromophoric in character with partial hybridization to environmental states. Notably, in the protein-embedded PSII-RC the LUMO+2 orbital is localized on the Q_B cofactor. This implies that the environment does not simply shift energies, but induces reordering of electronic states.

VI. Parameterized Results for $\epsilon^{-1}(k)$

The values reported in Table 12 are obtained from an isotropic fit to the k-space inverse dielectric function, $\epsilon^{-1}(k)$, derived from the screened exchange kernel $v_W(k)$. A graphical illustration of the fit is shown in Fig. 3. Definitions of the fitting parameters are given in Ref.[6]

Table 12: The resulting sets of the 7 fitted parameters of $\epsilon^{-1}(k)$ for isolated and protein-embedded PSII-RC systems.

	Isolated PSII-RC	**Embedded PSII-RC**
c_0	0.639	1.087
c_1	−2.875	−4.241
c_2	4.372	5.532
c_3	−2.678	−2.877
c_4	0.010	0.003
k_{mt}	0.820	0.740
γ	0.260	0.260

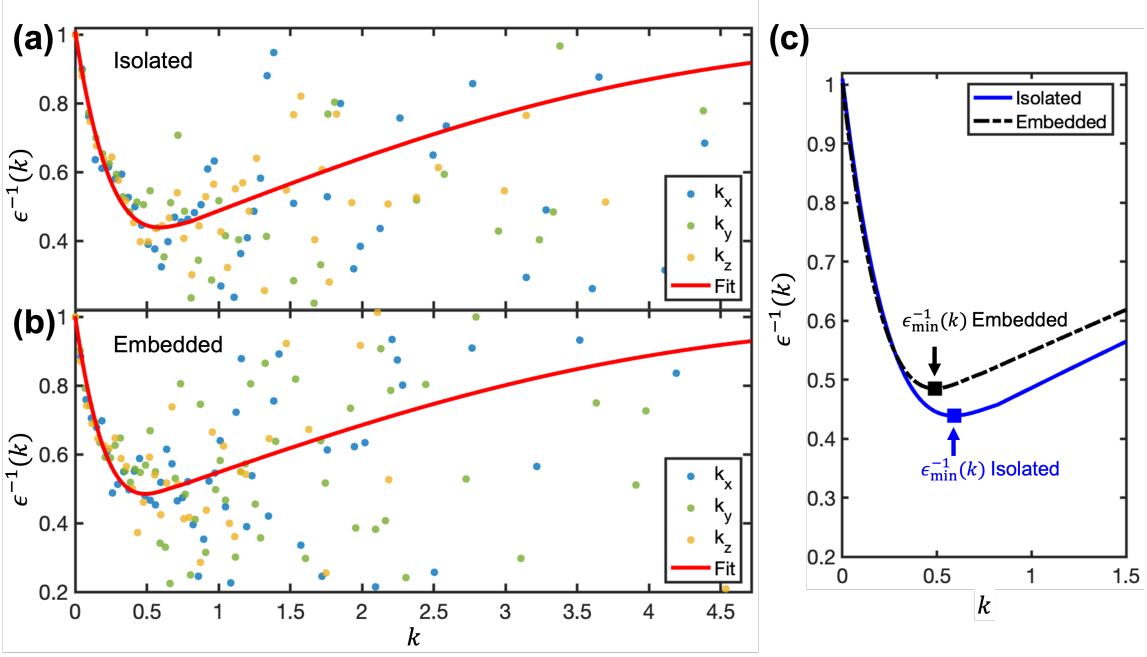

Figure 3: $\epsilon^{-1}(k)$ along $(1,0,0)$, $(0,1,0)$, and $(0,0,1)$ directions (dots) for the isolated **(a)** and protein-embedded PSII-RC **(b)**, k is in units of Bohr^{-1}, and the parameterization is in red lines. **(c)** shows the overlaid parameterizations, with the minimum k-space inverse dielectric value, $\epsilon^{-1}_{\min}(k) \equiv \min[\epsilon^{-1}(k)]$, for the isolated and protein-embedded PSII-RC labeled. These minima correspond to the real-space distances of 5.64 Å for the isolated system and 6.79 Å for the embedded system.

VII. Comparison of Full and TDA TDHF@v_W Spectra

To analyze the role of resonant-antiresonant coupling in large photosynthetic complexes, we provide TDA (Tamm-Dancoff approximation) spectra (Fig. 4) for both the isolated and embedded PSII-RC models. Within the TDA, the coupling matrix B in the Liouvillian operator is neglected. This halves the spectral range and requires half the number of required Chebyshev terms, with 1000 polynomials used in all TDA simulations.

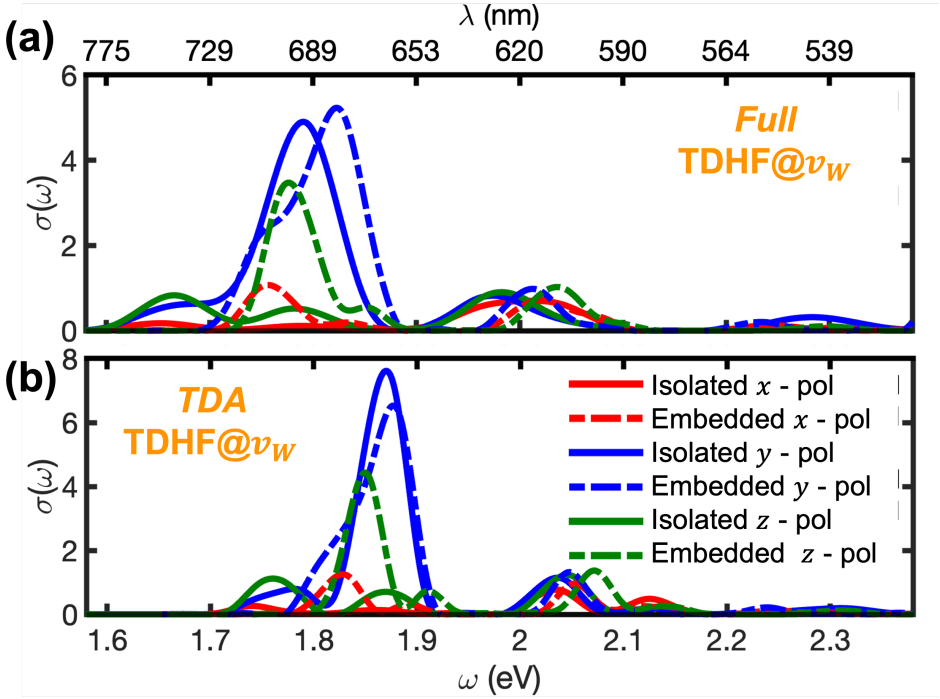

Figure 4: Full TDHF@v_W **(a)** and TDA **(b)** spectra for the isolated and protein-embedded PSII-RC. The same basis-set extrapolation parameters are applied to the TDA spectra.

References

1. Vlček, V.; Li, W.; Baer, R.; Rabani, E.; Neuhauser, D. Swift GW beyond 10,000 electrons using sparse stochastic compression. *Physical Review B* **2018**, *98*, 075107.

2. Bradbury, N. C.; Allen, T.; Nguyen, M.; Neuhauser, D. Deterministic/Fragmented-Stochastic Exchange for Large-Scale Hybrid DFT Calculations. *Journal of Chemical Theory and Computation* **2023**, *19*, 9239–9247.

3. Allen, T.; Li, B. Y.; Duong, T.; Williams, K.; Neuhauser, D. Efficient plane-wave approach to generalized Kohn-Sham density functional theory of solids with mixed deterministic and stochastic exchange. *Phys. Rev. B* **2025**, *112*, 155104.

4. Sereda, M.; Allen, T.; Bradbury, N. C.; Ibrahim, K. Z.; Neuhauser, D. Sparse-Stochastic

Fragmented Exchange for Large-Scale Hybrid Time-Dependent Density Functional Theory Calculations. *Journal of Chemical Theory and Computation* **2024**, *20*, 4196–4204.

5. Bradbury, N. C.; Li, B. Y.; Allen, T.; Caram, J. R.; Neuhauser, D. No more gap-shifting: Stochastic many-body-theory based TDHF for accurate theory of polymethine cyanine dyes. *The Journal of Chemical Physics* **2024**, *161*, 141101.

6. Li, B. Y.; Duong, T.; Allen, T.; Bradbury, N. C.; Caram, J. R.; Neuhauser, D. Parameterized attenuated exchange for generalized TDHF@v_W applications. *The Journal of Chemical Physics* **2025**, *163*, 034102.

7. Chen, K.; Li, B. Y.; Allen, T.; Neuhauser, D. Mixed Planewave and Localized Orbital Basis for Sparse-Stochastic Hybrid Time-Dependent Density Functional Theory. *Journal of Chemical Theory and Computation* **2025**, *21*, 8509–8517.

8. Neuhauser, D.; Gao, Y.; Arntsen, C.; Karshenas, C.; Rabani, E.; Baer, R. Breaking the Theoretical Scaling Limit for Predicting Quasiparticle Energies: The Stochastic GW Approach. *Physical Review Letters* **2014**, *113*, 076402.

9. Bradbury, N. C.; Nguyen, M.; Caram, J. R.; Neuhauser, D. Bethe–Salpeter equation spectra for very large systems. *The Journal of Chemical Physics* **2022**, *157*, 031104.

10. Bradbury, N. C.; Allen, T.; Nguyen, M.; Ibrahim, K. Z.; Neuhauser, D. Optimized attenuated interaction: Enabling stochastic Bethe-Salpeter spectra for large systems. *The Journal of Chemical Physics* **2023**, *158*, 154104.

11. Allen, T.; Nguyen, M.; Neuhauser, D. GW with hybrid functionals for large molecular systems. *The Journal of Chemical Physics* **2024**, *161*, 114116.

12. Negele, J. W. The mean-field theory of nuclear structure and dynamics. *Reviews of Modern Physics* **1982**, *54*, 913–1015.

13. Yanai, T.; Tew, D. P.; Handy, N. C. A new hybrid exchange–correlation functional using the Coulomb-attenuating method (CAM-B3LYP). *Chemical Physics Letters* **2004**, *393*, 51–57.

14. Weiße, A.; Wellein, G.; Alvermann, A.; Fehske, H. The kernel polynomial method. *Rev. Mod. Phys.* **2006**, *78*, 275–306.

15. Umena, Y.; Kawakami, K.; Shen, J. R.; Kamiya, N. Crystal structure of oxygen-evolving photosystem II at a resolution of 1.9 Å. *Nature* **2011**, *473*, 55–60.

16. Förster, A.; Visscher, L. Quasiparticle Self-Consistent GW-Bethe–Salpeter Equation Calculations for Large Chromophoric Systems. *Journal of Chemical Theory and Computation* **2022**, *18*, 6779–6793.

17. Bannwarth, C.; Caldeweyher, E.; Ehlert, S.; Hansen, A.; Pracht, P.; Seibert, J.; Spicher, S.; Grimme, S. Extended tight-binding quantum chemistry methods. *WIREs Computational Molecular Science* **2021**, *11*, e1493.

18. Neese, F. The ORCA program system. *WIRES Comput. Molec. Sci.* **2012**, *2*, 73–78.

19. Förster, A.; Visscher, L. Quasiparticle Self-Consistent GW-Bethe-Salpeter Equation Calculations for Large Chromophoric Systems. *Journal of Chemical Theory and Computation* **2022**,

20. Sirohiwal, A.; Neese, F.; Pantazis, D. A. Protein Matrix Control of Reaction Center Excitation in Photosystem II. *Journal of the American Chemical Society* **2020**, *142*, 18174–18190.

21. Martyna, G. J.; Tuckerman, M. E. A reciprocal space based method for treating long range interactions in ab initio and force-field-based calculations in clusters. *The Journal of Chemical Physics* **1999**, *110*, 2810–2821.